Influence of Magnetic Fields on a Defect-Complex in Group-III Nitride Semiconductors

Ishita Agarwal
Univeristät Bonn

October 2012

Contents

Chapter 1

Introduction

Group-III nitrides are direct wide band gap semiconductor. Together with ternary nitride alloys (e.g. AlGaN, InAlN, etc.) formed with other group-III nitride elements, they form a continuous alloy system whose direct optical bandgaps (from 0.7 eV to 6.2 eV) span the complete visible spectra and find wide spread applications in opto-electronics and high power transistors [Wu09]. AlN has high thermal stability and finds applications as substrates and housing for high temperature and high frequency devices. Al rich ternary compounds have been developed in the UV wavelength range with the promise of application as emitter and detectors (biological detectors, lighting, etc). AlN is the best substrate for producing the UV wavelength in the range of 210 nm needed for disinfection and hence, has a large market as water purifiers, biological disinfectant, etc. However, they need to be optimized for commercial use and research is being done in this direction. Because of the possible p-type and n-type doping in GaN, it is possible to make bright green, blue and white LEDs which have made LED displays and lighting possible. They find important application in data storage aswell (Blue-ray player, Cd writes and readers, etc.). Due to their vast potential, the group-III nitrides are of great interest and are extensively studied. Perturbed angular correlation (PAC) gives information about the microscopic crystal environment which makes it a perfect spectroscopic technique to study lattice diffusions and defect environments. In is also a group-III nitride making it the ideal probe to investigate AlN and GaN.

RBS/ channelling measurements show, approximately 95% of the In implanted in AlN occupy Al substitutional lattice sites [Lor02]. Past PAC measurements of ^{111}In in AlN [SNP+09] show two main lattice environments: a lattice fraction, where the In is at a defect free (undisturbed) substitutional Al site and exhibits a weak electric quadrupole interaction (QI); and a defect fraction, where a larger QI is assigned to a

complex between ^{111}In and a nearest neighbour nitrogen vacancy (V_N) aligned along the c-axis. Interestingly, the defect fraction shows a temperature dependence, the defect QI becomes weaker and its fraction reduces as the measuring temperature increases. At the critical temperature, T_c ∼1073 K it is not observed in favour of the lattice fraction and this effect is found to be completely reversible [SNP+09, LRV02]. However, the reason is still unclear. Another interesting observation is that the defect QI is not seen with ^{111m}Cd/^{111}Cd and ^{117}Cd/^{117}In probes, but only with ^{111}In/^{111}Cd. This implies that the defect is In specific [KLM+12]. Additionally, while the electric field gradient (EFG) of lattice fraction can be reproduced theoretically using the density function model (Wien2k code), a suitable configuration to describe the EFG of the defect fraction is yet to be found. By including spin-polarization in the calculations, a strong magnetic field at ∼50% of the ^{111}In/^{111}Cd site is expected. This could be an alternative explanation for the defect fraction and explain the strong QI. In this work, an attempt to understand the cause of the strong QI is made and thus, the possibility of a local magnetic field is investigated through different orientation measurements of the sample with and without an external magnetic field.

Chapter 2

Aluminium/Gallium Nitride Properties

Under normal conditions, AlN and GaN crystals have a wurtzite structure (Fig. 2.1) with a two atom base. It consists of two aligned hexagonal sub-lattices one each of Al/Ga and N shifted along the c-axis by u. The lattice is described by constants a, c and u. Ideally for AlN (and GaN), $u = 0.375$, but the real value for u is slightly larger corresponding to 0.382 (and 0.377). The relevant crystal properties are given in Table 2.1.

	AlN	**GaN**
Band gap[eV]	6.20	3.44
Lattice constant *a* [Å]	3.112	3.189
Lattice constant *c* [Å]	4.982	5.185
***u* - parameter**	0.382	0.377
Density [g cm^{-3}]	3.23	6.15

Table 2.1: Group-III nitride properties [Ins]

The wurtzite structure has a tetrahedral coordination with each atom surrounded by four nearest neighbours of the other sub-lattice. Since the tetrahedron here is not a perfect tetrahedron on account of unequal bond lengths along the a and c directions, there is a non-uniform charge distribution about the c-axis. This gives rise to an intrinsic electric field gradient (EFG) which is a tensor and whose principle component V_{zz} is axially symmetric about the c-axis.

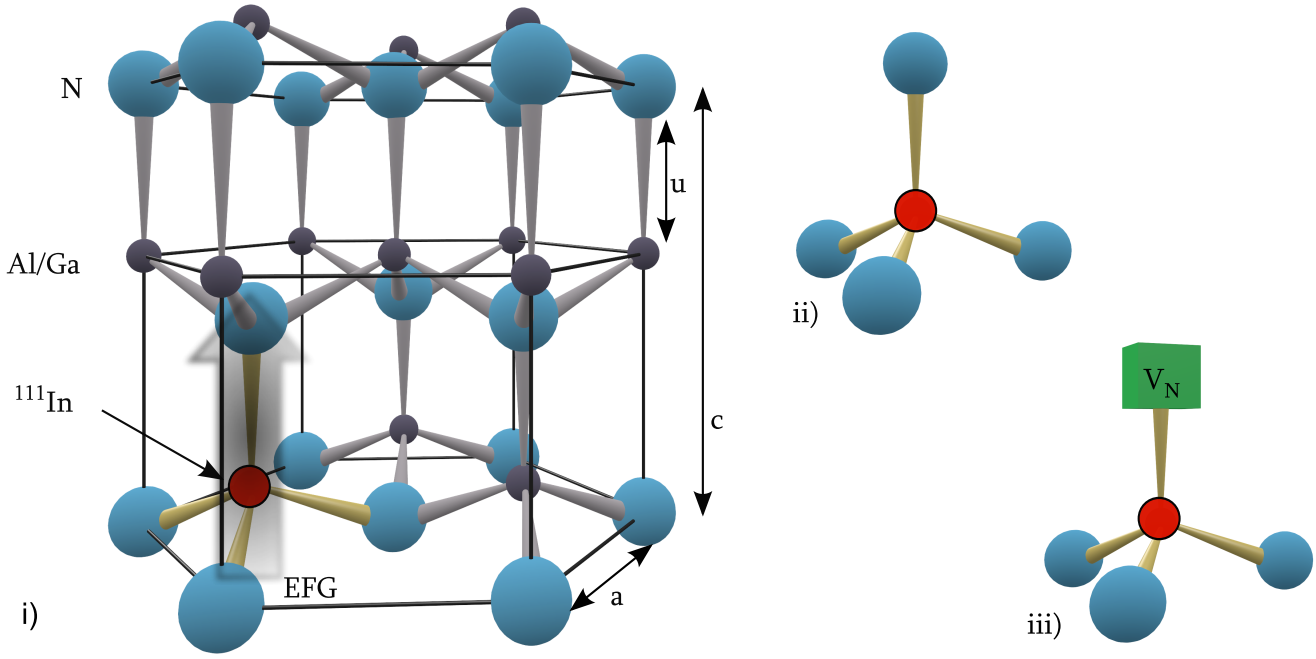

Figure 2.1: i) Ideal Wurtzite crystal structure of group-III nitrides. The small spheres represent Al and Ga atoms which are substituted with the implanted In. ii) a tetrahedron is the coordinate geometry in a wurtzite structure. iii) a nitrogen vacancy V_N aligned along the c-axis, cause of strong interaction in AlN and GaN

The samples used are prepared by Technologies and Devices International, Inc. (TDI), USA. They are grown on sapphire substrates with the crystal c-axis perpendicular to the polished surface. The AlN samples have a thickness of 0.7 μm and GaN have a thickness of 0.11 μm. Approximately (5×5) mm^2 pieces are used.

Chapter 3

Theoretical Background

3.1 Measurement Technique- Time Dependent Perturbed Angular Correlation Spectroscopy

Perturbed Angular Correlation (PAC) spectroscopy is used to investigate the microscopic crystal lattice environment. Information about phase change and transitions, defects and impurities- their production and lattice location, magnetism, etc. can be obtained. The technique involves the observation of an angular correlation between two γ-rays emitted in cascade from a decaying radioactive probe, time dependent in response to a hyperfine interaction between the probe nucleus and the electromagnetic lattice environment. To understand the concept behind PAC, first unperturbed angular correlation is explained and then perturbed angular correlation. Due to the complexity of the theory behind PAC, only the physical concept will be discussed below. For a detailed explanation, the book by Schatz and Weidinger [SW96] and K. Siegbahn [Sie65] should be referred to.

3.1.1 Unperturbed Angular Correlation

A radioactive isotope which decays to its stable state via emission of two particles (here, gammas) in a cascade, is introduced in the sample under investigation. Since the spin of the probe nuclei are randomly oriented in space, the γ emissions from the irradiated sample are isotropic. The pattern is anisotropic when γ_1 (Fig. 3.1) associated with $I_i \rightarrow I$ is detected in a preferential direction. A certain spin orientation is selected and all nuclei with this spin orientation contribute to the detected signal. By defining the z-axis in the direction γ_1, the selection rules is restricted to $\Delta m = \pm 1$ and γ_2 $(I \rightarrow I_f)$ is detected

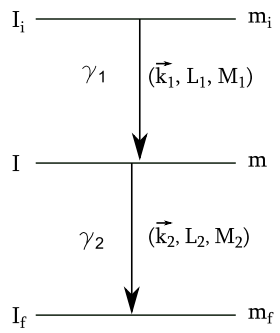

Figure 3.1: $\gamma - \gamma$ decay cascade scheme. I_i, I and I_f are the initial, intermediate and final states respectively with m_i, m and m_f the corresponding magnetic quantum numbers

anisotropically with respect to γ_1. Due to the correlation in their spatial distribution, it is called *angular correlation*.

The term of interest is the angular correlation function which gives the probability of observation of γ_2 in $\vec{k}_2$ direction when γ_1 is emitted in $\vec{k}_1$ direction via the $I_i \to I \to I_f$ cascade. It is expressed as:

$$W(\vec{k_1}, \vec{k_2}) = \sum_{m_i, m_f} \left| \sum_{m} \langle m_f \mid H_2 \mid m \rangle \langle m \mid H_1 \mid m_i \rangle \right|^2 \tag{3.1}$$

where,

$$\langle m \mid H_1 \mid m_i \rangle = \langle I, m, \vec{k}_1, \sigma_1 \mid H_1 \mid I_i, m_i \rangle \tag{3.2}$$

$$\langle m_f \mid H_2 \mid m \rangle = \langle I_f, m_f, \vec{k}_2, \sigma_2 \mid H_2 \mid I, m \rangle \tag{3.3}$$

and m is the magnetic quantum number, σ_1 and σ_2 are polarizations of the two gammas and $H_{1/2}$ is the interaction Hamiltonian. The deviation of the angular correlation from the isotropic distribution is given by the anisotropy coefficient A_{kk}, described as:

$$A_{kk} = A_k(1) A_k(2) \tag{3.4}$$

where k takes the values from

$$0 \leq k \leq \text{minimum of } (2I, L_1 + L_1', L_2 + L_2') \tag{3.5}$$

$A_k(1)$ and $A_k(2)$ are orientation coefficients and depend on γ_1 and γ_2 respectively. I is the spin of the intermediate state, L and L' are the multipolarities of the radiations. After calculating the matrix elements, the angular correlation function becomes:

$$W(\theta) = 1 + \sum_{k_{even} \neq 0}^{k_{max}} A_{kk} P_k(\cos\theta) \tag{3.6}$$

where θ is the angle between the two gammas (Fig. 3.2) and $P_k(\cos\theta)$ is a Legendre polynomial.

3.1.2 Perturbed Angular Correlation (PAC)

In the presence of an electromagnetic field, the nuclear moments interact with the extranuclear field and hyperfine interaction takes place. This lifts the degeneracy from the intermediate decay level I and the population of the m-substate sees fluctuations. Consequently, γ_2 is emitted in a direction different from that without the field and the angular distribution changes. It becomes time dependent and reflects the dynamic population changes in the m-sublevel. That is,

$$W(\theta, t) \sim \sum_{k_{even}}^{k_{max}} A_{kk} G_{kk}(t) P_k(\cos\theta) \tag{3.7}$$

where $G_{kk}(t)$ is the perturbation function. It contains all the perturbation information including the hyperfine interaction (time dependency).

The population change from an initial sublevel $\mid m_a\rangle$ to a final sub-level $\mid m_b\rangle$ is given by a time evolution operator, $\Lambda(t)$ which is an unitary operator. It satisfies the Schrödinger equation and is described by the interaction Hamiltonian H. For static perturbation:

$$\Lambda(t) = \exp(-iHt/\hbar) \tag{3.8}$$

After substituting Eq. 3.8 in Eq. 3.1 and further calculations, $W(\theta, t)$ for a static extranuclear field can be written as:

$$W(\vec{k_1}, \vec{k_2}, t) = \sum_{k_1 k_2 N_1 N_2} A_{k_1}(1) A_{k_2}(2) G_{k_1 k_2}^{N_1 N_2}(t) [(2k_1+1)(2k_2+1)]^{-\frac{1}{2}} \times Y_{k_1}^{N_1^*}(\theta_1, \phi_1) Y_{k_2}^{N_2}(\theta_2, \phi_2) \tag{3.9}$$

where Y_k^N are spherical harmonics and the polar angles θ and ϕ are shown in Fig. 3.2. k_1 and k_2 fulfil the condition given by eq. (**??**) and N_1 and N_2 take values between $-k$ and $+k$. The perturbation function is given by:

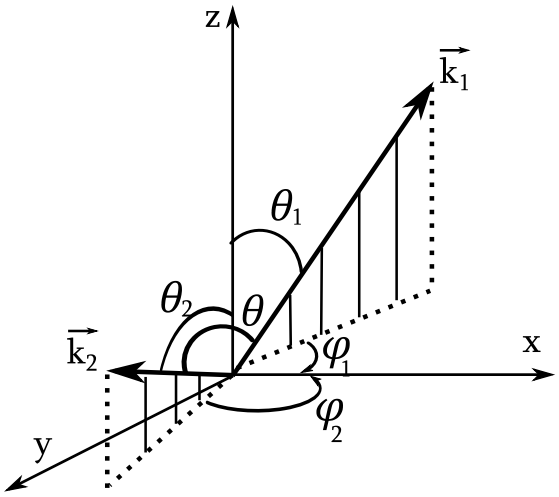

Figure 3.2: Polar spherical angles showing the spatial orientations of γ_1 and γ_2. γ_1 decays in the direction of $\vec{k}_1$ and γ_2 in the direction of $\vec{k}_2$. The angle between γ_1 and γ_2 is given by θ [Lor02]

$$G_{k_1 k_2}^{N_1 N_2} = \sum_{m_a m_b} (-1)^{(2I+m_a+m_b)} [(2k_1+1)(2k_2+1)]^{\frac{1}{2}} \begin{pmatrix} I & I & k_1 \\ m_a' & -m_a & N_1 \end{pmatrix} \times \begin{pmatrix} I & I & k_2 \\ m_b' & -m_b & N_2 \end{pmatrix} \langle m_b \mid \Lambda(t) \mid m_a \rangle \langle m_b' \mid \Lambda(t) \mid m_a' \rangle^* \tag{3.10}$$

For fields axially symmetric about the z-axis:

$$\langle m_b \mid \Lambda(t) \mid m_a \rangle = \exp\left(-\frac{i}{\hbar} E_m t\right) \delta_{m,m_a} \delta_{m,m_b} \tag{3.11}$$

where $m_a = m_b =: m$ and $m_a' = m_b' =: m'$.

Substituting Eq. 3.11 in Eq.3.10:

$$G^{NN}_{k_1k_2} = \sum_{m_a m_b} (-1)^{(2I+m_a+m_b)}[(2k_1+1)(2k_2+1)]^{\frac{1}{2}} \begin{pmatrix} I & I & k_1 \\ m'_a & -m_a & N_1 \end{pmatrix} \times \begin{pmatrix} I & I & k_2 \\ m'_b & -m_b & N_2 \end{pmatrix} \exp\left[-\frac{\iota}{\hbar}\left(E_m - E_{m'}\right)t\right] \tag{3.12}$$

$$G_{kk}(t) \sim \exp(-i\omega t) \sim \exp\left[-\frac{i}{\hbar}(E_m - E'_m)t\right] \tag{3.13}$$

where $N_1 = N_2 =: N$ and ω is transition frequency between the m-substates. Eq. 3.13 shows, the perturbation function is dependent on the energy difference between the m sublevels, and intern these difference can be determined.

Electric Quadrupole Interaction:

The electric field gradient (EFG) is a second partial derivative of the electrostatic potential and is given by:

$$V_{ij} = \frac{\partial^2 V(\vec{r})}{\partial x_i \partial x_j} \qquad i,j = 1,2,3 \tag{3.14}$$

It is generated due to the crystal geometry and interacts with the quadrupole moment Q of the nucleus. It is a second order tensor and by diagonalizing it by a suitable choice of the coordinate system, only the three diagonal elements are non-zero. Conventionally, V_{zz} is the largest of the non-zero diagonal elements V_{xx}, V_{yy} and V_{zz}. As these diagonal elements fulfil the Poisson equation, there are only two independent quantities fully describing the EFG. The asymmetry parameter $\eta = (V_{xx} - V_{yy})/V_{zz}$ is zero when the EFG is axially symmetric (example wurtzite structure).

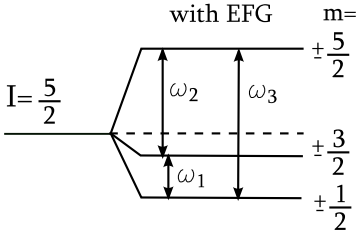

Figure 3.3: Hyperfine splitting of the intermediate level I for spin 5/2 due to an extranuclear EFG

The interaction Hamiltonian is diagonal for $\eta = 0$ and the energy differences between the individual substates is given by the difference in the eigenvalues E_m by:

$$\Delta E = E_m - E_{m'} = \frac{3eQV_{zz}}{4I(2I-1)} \mid m^2 - m'^2 \mid \tag{3.15}$$

The quadrupole interaction (QI) is described by the quadrupole frequency ω_Q

$$\omega_Q = \frac{eQV_{zz}}{4I(2I-1)\hbar} \tag{3.16}$$

The energy splitting can now be expressed in term of the quadrupole frequency as:

$$\delta E = 3\hbar\omega_Q \mid m^2 - m'^2 \mid \tag{3.17}$$

The smallest observable transition frequency is related to ν_Q by:

$$\omega_0 = 3\omega_Q = \frac{3eQV_{zz}}{4I(2I-1)\hbar} \qquad \text{for half integer spin} \tag{3.18}$$

and higher QI frequencies in the case of axially symmetric perturbation for spin $I = \frac{5}{2}$ (in the case for ^{111}In, Fig. 3.3) is given as:

$$\omega_n = n\omega_0 = 3n\omega_Q \qquad\qquad n = 1, 2, 3 \tag{3.19}$$

where n is an integer multiple. More explicitly:

$$\begin{aligned} \omega_1 &= 1\omega_0 = 3\omega_Q \\ \omega_2 &= 2\omega_0 = 6\omega_Q \\ \omega_3 &= 3\omega_0 = 9\omega_Q \end{aligned} \tag{3.20}$$

The strength of the quadrupole interaction at the probe site is given by the quadrupole coupling constant ν_Q. It is independent of spin and characterises the crystal EFG. For spin 5/2, it is defined as:

$$\nu_Q = \frac{eQV_{zz}}{h} = \frac{3\pi}{10}\omega_0 = 1.06\omega_0 \tag{3.21}$$

The perturbation factor for axially symmetric QI can be written as:

$$G_{k_1k_2}^{NN} = \sum_{m_a m_b} (-1)^{(2I+m_a+m_b)} \sqrt{(2k_1+1)(2k_2+1)} \begin{pmatrix} I & I & k_1 \\ m' & -m & N \end{pmatrix} \times \begin{pmatrix} I & I & k_2 \\ m' & -m & N \end{pmatrix} \exp\left[-\frac{3i}{\hbar}(m^2 - m'^2)\omega_Q t\right] \tag{3.22}$$

$$= \sum_n s_{nN}^{k_1k_2} \cos(n\omega_n t) \tag{3.23}$$

where $s_{nN}^{k_1k_2}$ is the amplitudes of the transition frequencies. It is determined by the spin of the intermediate level and depends upon η and the angle between k_1 and k_2. Hence, the perturbation function depends on the EFG (and the crystal) orientation. This is discussed in detail in Section 3.1.

From the above equation, it is seen, the perturbation factor is a superposition of cosine functions. The individual perturbation functions corresponding to single transition frequencies depend on the spherical harmonics (Eq. 3.9). As a result, the effective amplitudes s_{nN}^{eff}, and the angular correlation function reduces to:

$$W(\theta, t) = 1 + A_{22} \sum_{n=0}^{3} s_n^{eff}(\theta_1, \phi_1, \theta_2, \phi_2) \cos(n\omega_1 t) \;=\; 1 + A_{22}\tilde{G_{22}}(t) \tag{3.24}$$

Magnetic Dipole Interaction

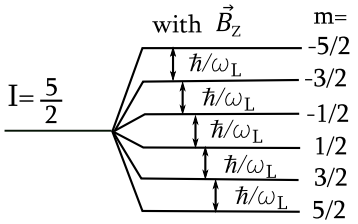

Figure 3.4: Equivalent hypefine splitting of spin 5/2 intermediate I state due to an external magnetic field $\vec{B}_Z$ parallel to the z-axis

The nuclear dipole moment of the probe atom interacts with a surrounding magnetic field $\vec{B}_{ext}$ through Zeeman interaction. The resulting energy difference between the

m-sublevels is:

$$E_m - E_{m'} = -(m - m')g\mu_N B_Z = \hbar\omega_L \tag{3.25}$$

where $m - m' = 1$ for neighbouring transitions. $\omega_L = g\mu_N B_Z/\hbar$ is the corresponding Larmor frequency (Fig. 3.4), g is the g-factor and μ_N is the nuclear magneton. Eq. 3.25 in Eq. 3.12:

$$G^{NN}_{k_1 k_2} = \sum_m \sqrt{(2k_1+1)(2k_2+1)} \begin{pmatrix} I & I & k_1 \\ m' & -m & N \end{pmatrix} \times \begin{pmatrix} I & I & k_2 \\ m' & m & N \end{pmatrix} \exp[-i(m-m')\omega_L t] \tag{3.26}$$

which on calculation of the 3-j symbols and further simplification yields:

$$G^{NN}_{kk}(t) = \exp[-i(m-m')\omega_L t] \tag{3.27}$$

This shows, the angular correlation process at Larmor frequency and higher harmonics of $(m - m')\omega_L$. Summing over N and plugging Eq. 3.26 in Eq. 3.10, we get:

$$W(\theta, t) = \sum_k A_k(1) A_k(2) P_k(\epsilon) \tag{3.28}$$

where

$$\epsilon = \cos\theta_1 \cos\theta_2 + \sin\theta_1 \sin\theta_2 \cos(\theta - \omega_L t), \quad \theta = \Delta\phi = \phi_2 - \phi_1 \tag{3.29}$$

Here too, an orientation dependence of the magnetic field with the direction of γ-emission is seen.

Combined interaction

In the presence of both, magnetic and electric interaction, the interaction Hamiltonian is given as:

$$H = H_{EFG} + H_{magnet} \tag{3.30}$$

and is defined as:

$$H_{mm'} = \hbar\omega_Q\{-ym\delta_{mm'} + \left(\frac{\pi}{5}\right)^{1/2}(-1)^{I-m}\sqrt{(2I+3)(2I+2)(2I+1)2I(2I-1)} \times \begin{pmatrix} I & 2 & I \\ -m & m-m' & m' \end{pmatrix} Y_2^{m'-m}(\beta,\alpha)\} \tag{3.31}$$

For $I = 5/2$, the Hamiltonian is a 6×6 matrix which on diagonalization gives six eigenvalues E_n. Using these, all possible transitions between the m-substates is determined. An anti-symmetric matrix representing the corresponding 36 possible transition frequencies is obtained of which, the six diagonal elements ω_{nn} are the zero frequency transitions. Since, $\omega_{nN} = -\omega_{Nn}$ and hence, $\cos(\omega_{nN}t) = \cos(\omega_{Nn}t)$, there are 15 distinct frequency magnitudes. From references [KAN53, KAS63, MSS62], the perturbation function is given by:

$$G^N_{k_1k_2} = \frac{1}{2}\sum_n a^{k_1k_2}_{nN}\left[\frac{1}{1+(n\omega_Q\tau + N\omega_L\tau)^2}H(n\omega_Q\tau + N\omega_L\tau) + \frac{1}{1+(n\omega_Q\tau - N\omega_L\tau)^2}H(n\omega_Q\tau - N\omega_L\tau)\right] \tag{3.32}$$

where $a^{k_1k_2}_{nN}$ is again the weighting factor. The perturbation function above cannot be solved analytically and have to be computed. The angular correlation function strongly depends on η, β (orientation of the magnetic field direction with V_{zz}), y $(= \omega_L\backslash\omega_Q$, ratio of Larmor frequency to the quadrupole interaction) and α (a second Euler angle) shown in the work done by [KAS63].

Due to overlapping sine and cosine terms, the analysis of combined interaction is very complex. In the R(t) spectra, the weaker interaction modulates/damps the dominant interaction. For example, when the QI is dominant (much stronger compared to the magnetic field), the corresponding ω is observed which is damped by ω_L corresponding to the magnetic hyperfine interaction. For fields in the same range, both the sine and cosine terms take equal preference and a superposition of the two is seen

3.2 Orientation Dependence

As mentioned in the previous sections, ω_n are weighted by $s_{nN}^{k_1 k_2}$ and, for $I = 5/2$ and $\eta = 0$, ω_1, ω_2 and ω_3 are observed. Because s_{nN} depends on the orientation of the EFG, at different crystal orientations, a different principle frequency is seen [KAN53, RR71]. The dependence of these frequencies on the EFG orientation is given in Table 3.1 generated using the software Nightmare (Section 4.2). The orientation angles in the Table are described in Fig. 3.5

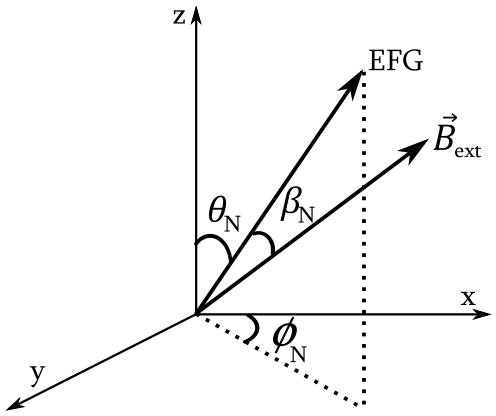

Figure 3.5: Spherical representation of the crystal EFG and the applied magnetic field. Note, these angles are adopted by NIGHTMARE's fit routine and are completely different from those described in Fig. 3.2

Angle(ϕ_N, θ_N)	S_{21}	S_{22}	S_{23}	ω_n
0°, 0°	0	0	0	-
45°, 0°	0.29	0.71	0	ω_2
0°, 90°	0.64	0	0.36	ω_1

Table 3.1: Dependence of S_{2n} on the orientation of an axially symmetric EFG for 5/2 spin. S_{21} weights ω_1, S_{22} weights ω_2 and so on. The last column in the table gives the principle frequency. For $\phi_N = 45°$, S_{23} is dominant and ω_3 is the principle frequency, but for $\theta_N = 90°$, S_{21} is the dominant amplitude and hence, ω_1 is the principle frequency

A magnetic dipole hyperfine interaction is characterized by only one frequency, ω_L (Larmor frequency). When the magnetic dipole is oriented 45° to the start detector in the detector plane, ω_L is observed, whereas, when oriented perpendicular to the detector plane, $2\omega_L$ is seen [RR71]. Like in the case of an EFG, when the magnetic

dipole is oriented parallel to the start detector, no change in correlation is observed by the detectors and no frequency is observed. This helps in identifying the orientation of the internal fields.

3.3 ^{111}In Probe

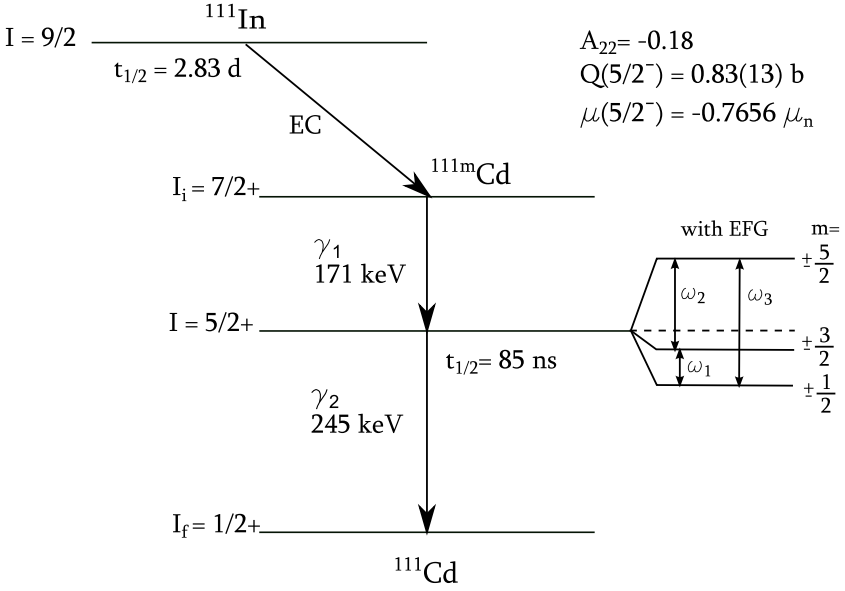

Figure 3.6: Decay scheme of ^{111}In

Radioactive ^{111}In isotope is used as the probe in this work. It decays to stable ^{111}Cd via electron capture through emission of two γ-rays in a cascade. Fig. 3.6 shows the decay scheme. The intermediate level has a spin $I = 5/2$, suitable for γ-γ PAC measurements. ^{111}In due to the spin 5/2 intermediate state observes $n = 3$ in ω_n for QI and observes three possible transition frequencies. For magnetic interaction, it splits with five possible equal transitions of ω_L.

The half life of the intermediate level is 85 ns which lies in the ideal range between 10 ns to several μs [SW96] for PAC measurements. It is larger than the time resolution of the measuring apparatus and short enough to have a high signal-to-noise ratio. Its quadrupole moment $Q(5/2^+) = 0.83$ barn is large enough for investigating EFG. However, its magnetic dipole moment $\mu(5/2^+) = -0.76\ \mu_N$ is not very large (^{100}Pd has a bigger μ_N) and is not the ideal probe to study magnetic investigation. But since we are interested in investigating In in AlN, we still use it for studying the effect of external magnetic

fields. The half life of the ^{111}In parent isotope is 2.83 days, giving time for multiple measurements with the same sample.

The probe, ^{111}In was implanted at the Bonn Radioisotope Separator and Implanter (BONIS), Bonn. The implantations were done at an angle of incidence of 12° (to avoid channelling) with an energy of 80 keV and the fluence $\sim 10^{12}$ ions/cm^2. The implantation depth is estimated to be 30 nm from the surface by SRIM 2008 calculations [BH80].

Chapter 4

Experimental Setup

4.1 PAC Setup

All the measurable information about the hyperfine interaction is contained in the perturbation function as shown in Section 3.1. This information is obtained by measuring the coincidence count rate of the two subsequent gammas as a function of time.

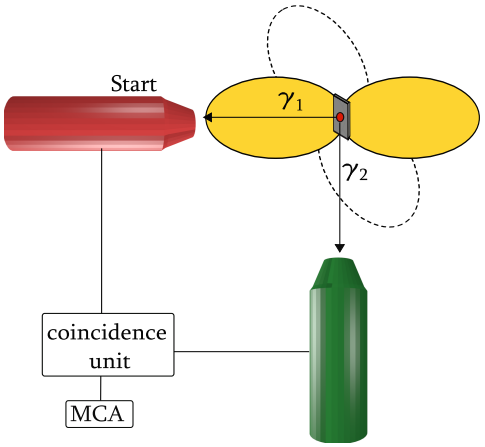

Figure 4.1: A two detector PAC setup with the detectors in the same plane and perpendicular to each other. The start detector observes γ_1 and provides the start signal to the TAC and the other detector(s) observe γ_2 and provide the stop signal

Fig. 4.1 depicts a simplified PAC setup. Here two detectors are arranged in fixed positions 90° to each other and record the coincidences between the two gammas. Due to perturbation, the emission pattern of γ_2 oscillates with time and the coincidence count rate changes periodically. The detectors are scintillation crystals mounted on photomultiplier tubes. In the following work a 4-detector and a 3-detector setup is used. In the 4-detector setup, four detectors are fixed at a 90° interval in a plane and in the

3-detector setup, two detectors are fixed at 90° and a third detector is movable (can be aligned 90° or 180° to the other two detectors).

The Spectrometer is based on the fast-slow coincidence method. The fast signal contains timing information and is converted into a logical signal by the constant fraction discriminator (CFD) [ZJ11]. The logical output provides the start and stop signal for the time to amplitude converter (TAC). The TAC measures the time elapsed between the first and the second gamma with the help of the start and stop signals and generates a pulse whose height corresponds to the elapsed time. The signal is sent to an analog-to-digital converter (ADC) which converts the TAC output into a digital representation. The slow signal contains energy information and is sent to the single channel analyser (SCA). The SCA checks the gammas with the right cascade energy and only permits them to contribute to the PAC spectra. A routing unit checks if the two gammas are from the same nuclei. When this is the case, the ADC gets a signal to record the data in the appropriate memory bank of the multichannel-analyser (MCA). A schematic diagram of the data reduction scheme is shown in Fig. 4.2. A detailed description of the detecting circuit and its working can be found in [AHP+80].

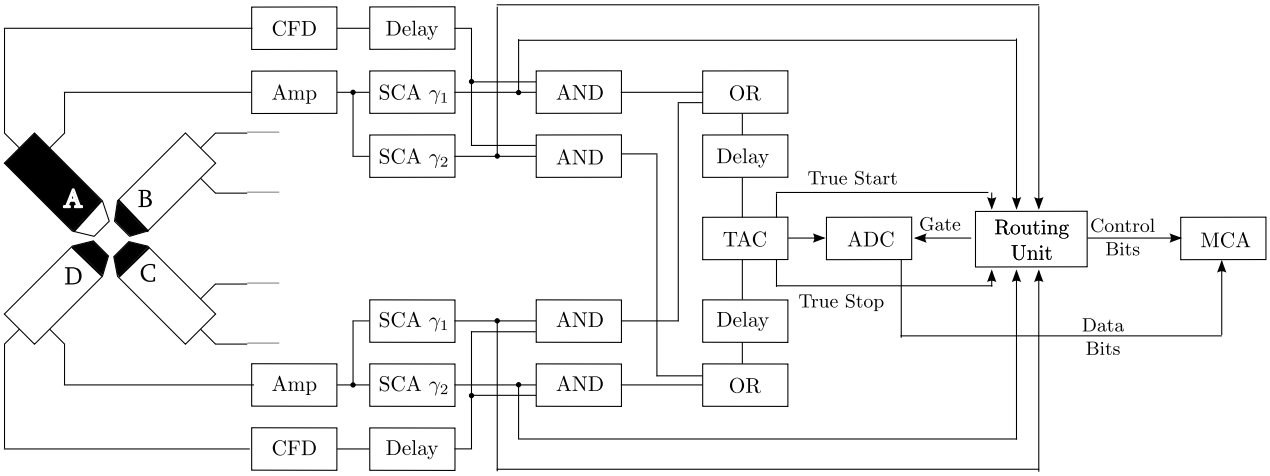

Figure 4.2: A schematic diagram of the fast-slow coincidence circuit used. For simplicity only the electronics for two detectors are shown. Each detector is associted with a photomultiplier which generates the fast and slow signal. Adapted from [Sim11]

The coincidences occurring in detectors i and j at angle θ_{ij} are a sum of, 1) true coincidences, $N_{ij}(\theta_{ij}, t)$ where the two detected photons are from the same nuclei, and 2) accidental coincidence, $B_{ij}(\theta_{ij}, t)$ where, the photons are from different nuclei. Accidental coincidences contribute to the time-independent background. For axially symmetric and

randomly oriented fields, the angular correlation (given by Eq. 3.7) is,

$$W(\theta, t) = 1 + A_{22}G_{22}P_2(\cos(\theta)) + ... \tag{4.1}$$

The true coincidences are given by:

$$N_{ij}(\theta_{ij}, t) = N_{0,ij} \exp\left(\frac{-t}{\tau}\right) W(\theta_{ij}, t) \tag{4.2}$$

$$= N_{0,ij} \exp\left(\frac{-t}{\tau}\right) (1 + A_{22}G_{22}(t)) \tag{4.3}$$

where $N_{0,ij}$ is the source activity and τ is the mean lifetime of the intermediate level.

After subtracting the background $B_{ij}(\theta_{ij}, t)$, the perturbation function can be extracted from Eq. (4.2) by constructing a counting ratio R(t), given by:

$$R(t) = 2\frac{\bar{N}(180°, t) - \bar{N}(90°, t)}{\bar{N}(180°, t) + 2\bar{N}(90°, t)} \tag{4.4}$$

$$\tag{4.5}$$

where $\bar{N}(\theta, t)$ is the geometric mean of the background corrected coincidence count rates.

R(t) is the normalized difference of true coincidences between two different angles and is considered as the PAC spectrum. For $\mid A_{44} \mid \ll 1$:

$$R(t) = A_{22}G_{22}(t) \tag{4.6}$$

Since the detector efficiencies and solid angle appear in both the numerator and the denominator of the above equation, they cancel out, making the four detector arrangement very convenient. Each detector is used as a start and stop detector recording 12 coincidence spectra. The coincidence counts for the same angle are averaged and the count rate is determined.

The time calibration of the time to amplitude converter (TAC) is found by using a *flugzeit generator*. The number of channels in 20 ns for 1.6 μs is calculated. Also, the time resolution of the spectra is needed. The ^{111}In spectra are broadened due to finite

time resolution and are described by Gaussian distribution. Therefore, for more accuracy, zeroth time points are set by using a ^{60}Co source which has well defined prompt curves.

4.2 Data Analysis

The R(t) function is obtained using the software ShowFit [Rus01]. Since there is more than one perturbation due to different lattice environments, the measured perturbation function $G(t)$ is a linear superposition of the individual perturbation function, $G_i(t)$:

$$G(t) = \sum_i f_i G_i(t) \qquad \text{and} \qquad \sum_i f_i = 1 \tag{4.7}$$

where f_i is the fraction of the probe subjected to $G_i(t)$

The PAC spectrum is fitted using the programme Nightmare version RC 3 (1.2.0.247) [NÓ7] based on NNFit routine [Bar92] Parameters used to fit the ratio function by least square method are:

Quadrupole frequency, ω_0 [MHz] gives information about the different EFG strengths.
Larmor frequency, ω_L [MHz] gives the strength of magnetic interaction with the probe nuclei.
Crystal fraction, f[%] gives the amplitude of the frequency and denotes the fraction of the probes exposed to a particular crystal environment.
Damping factor, δ[%] gives the width of the frequency and is due to imperfections in the crystal which result in a broadening of the frequency in the Fourier space.
Asymmetry parameter, η.

In case of extranuclear electric fields, there are three crystal orientation parameters, **theta θ_N**, **phi ϕ_N** and **rho ρ_N**. θ_N and ϕ_N are the angles made by the pointing tensor, V_{zz} of the EFG with the detector plane and with the detector in the detector plane respectively (not to be confused with θ and ϕ in Fig. 3.2). ρ_N is used to fit the asymmetry in the EFG. For external magnetic field, there are two orientation parameters, **beta β_N** and **gamma γ_N** which are the relative orientations of the magnetic field with the EFG about the V_{zz} and about V_{yy} respectively. The probe environment can be characterised as single crystalline or polycrystalline. The damping is Lorentzian in ω_0.

4.3 Magnet Pot

A specially designed magnet pot (Fig. 4.3) is used to provide a uniform magnetic field, $\vec{B}_{ext}$ [MÖ9]. It consists of a semi-hollow 2 cm Trovidur cylinder in which the sample is held with the help of two slits. (5×5) mm^2 samples can fit inside comfortably. It is encased in a thin iron sheet which guide the magnetic field lines through it and concentrate the field nearer the magnet pot. In this way the detectors are protected from the stray magnetic field lines. Two identical cylindrical permanent magnets can be placed in the holes at the top and bottom of the Trovidur cylinder separated by a distance of 6 mm. In the following, a pair of magnets with a $\vec{B_{ext}} = 0.48(5)$ T ...are used.

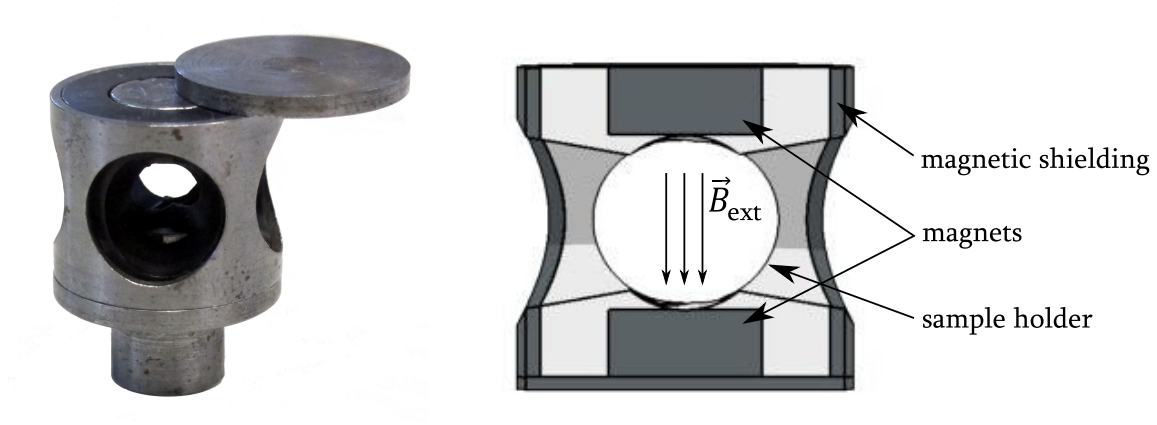

Figure 4.3: Left: image of the magnet pot with the 0.5 T magnets. Right: cross section diagram

Since the energies of the emitted gammas in the case of ^{111}In are 171 keV and 245 keV, they are absorbed by the iron shielding and due to scattering, anisotropy is reduced. Four holes at 90° angles were drilled into the walls of the Trovidur cylinder and the iron shielding. By arranging the magnetic pot such that the holes face the detectors during measurement, the absorption and scattering is reduced. The holes were drilled such that they were 45° to the sample.

For measurements in 2.1 T magnetic field [ABH+93], a bigger magnet pot shown in Fig. 4.4 is used. Two cylindrical permanent magnets made of Vacodym 362HR (Nd_2Fe_16B-matrix) are housed in a cylinder made of a combination of aluminium, lead and Armco iron. The housing also shields the detectors from the magnetic field lines in te same way as the iron sheet in the 0.5 T magnet pot. The gap between the two magnets is 2.4 mm in which a magnetic field strength of 2.1 T is produced. There are 12 radial windows around the cylindrical pot to reduce absorption and scattering. Due to the small gap,

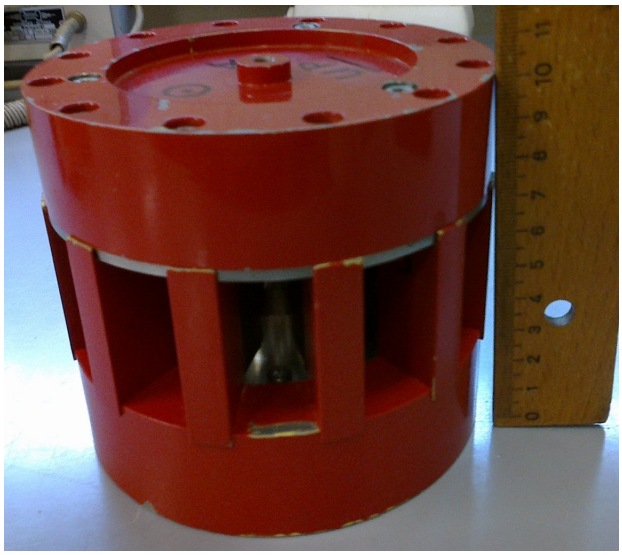

Figure 4.4: 2.1 T magnet pot

the sample size is restricted. Further, the magnet pot has a radius of 5 cm because of which, the closest the detectors can be place to the sample is a little more than 5 cm greatly decreasing the statistics. Additionally, Lead used in the housing absorbs gammas, further decreasing the statistics. Hence, very strong samples are needed to measure in this magnet pot. Due to the metal present in the housing, there is a lot of scattering which reduces the anisotropy.

Chapter 5

Measurements

The samples were first implanted with the radioactive In as described in section 3.3. Consequently, they incur a lot of damage due to radiations and need to be recovered. Therefore, the AlN and GaN samples were annealed in a RTA device at 1250 K for 10 minutes in N_2 flow with a proximity cap of the same material. The implantation and annealing conditions are the same for all the samples.

RBS/ channelling measurements show, approximately 95% of the In implanted in AlN and GaN occupy Al and Ga substitutional lattice sites respectively. Past PAC measurements of ^{111}In in AlN and GaN show three lattice environments:
a **lattice fraction**, where the In is at an undisturbed substitutional Al (Ga) site and exhibits a weak QI with quadrupole coupling constant of $\nu_Q^{lattice} \approx 30$ MHz;
a **defect fraction**, which is tentatively assigned to a complex between ^{111}In and a nearest neighbour nitrogen vacancy (V_N) aligned along the c-axis with a larger QI of $\nu_Q^{def} \approx 300$ MHz;
and an **asymmetry fraction**, also with a weak QI ($\nu_Q^{asym} \approx 35$ MHz) but is due to a second nearest V_N defect. The asymmetry fraction is found to have η from 0.4 - 0.6.

In order to account for the strong interaction (defect fraction), from spin polarization calculations in the DFT model, a $\nu_Q^{def} \approx 65$ MHz and ω_L^{def} of ≈ 206 MHz is estimated for AlN. The defect fraction is of interest to us and is the focus of this work. Hence, most of the discussions will pertain to the defect fraction.

5.1 AlN

5.1.1 Observations

We exploit the dependence of the observed frequency in the PAC spectra on the orientation of the EFG/magnetic dipole with the start detector (Section 3.2).

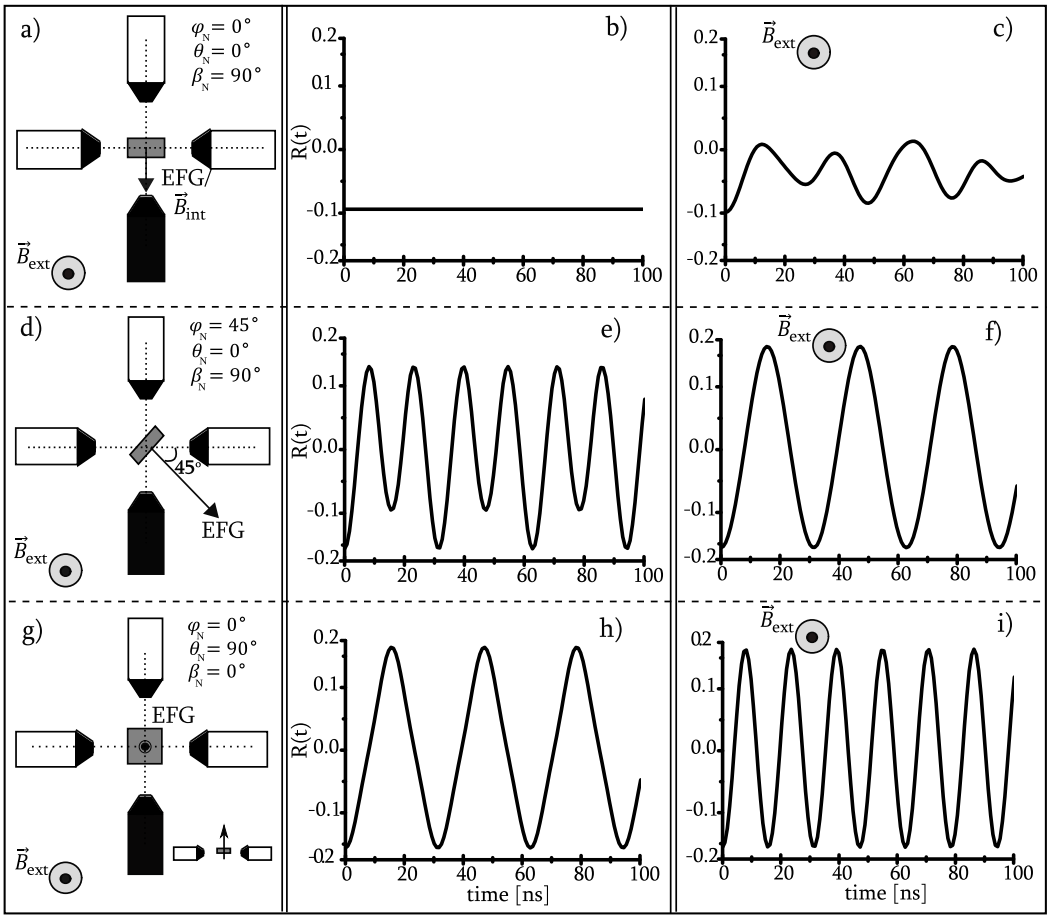

Figure 5.1: (i) different crystal orientations investigated in this work, (ii) corresponding simulated spectra for QI generated, (iii) simulated spectra for magnetic dipole interaction. $\vec{B}_{int}$ in a) corresponds to an internal magnetic field. The spectra are generated using the NIGHTMARE software

Three different sample orientations are investigated in this work. Fig. 5.1 depicts the different EFG orientations and the simulated R(t) spectra. In the first case, the c-axis is parallel to the start detector, Fig. 5.1 a-c). In Fig. 5.1 b), the simulation is done for an EFG and a magnetic field separately pointing at the start detector. Since for both, no

change in correlation is detected, no frequency is seen. In Fig. 5.1 c), the simulation is performed for a magnetic field oriented perpendicular to the detector plane (comparable ω_0 and ω_L). In this case, the corresponding frequency is observed. In the second case, the c-axis is oriented 45° to the start detector in the detector plane, Fig. 5.1 d-f). For quadrupole interaction, a frequency of ω_2 is seen but for dipole interaction, ω_1 is seen. In the third case, the c-axis is perpendicular to the detector plane, (Fig. 5.1 g-i). For quadrupole interaction, a frequency of ω_1 is seen and for dipole interaction, ω_2 is seen [Bez98, Lor02, RR85]. On the basis of this orientation dependence on the type of interaction, the data is analysed.

c-axis || Start Detector

In order to determine the orientation of the EFG and the possible magnetic interaction, measurements were done in the past with the c-axis pointing at the start detector (in the absence of any external field), Fig. 5.2 left. In the R(t) spectra, no frequency is observed. This establishes that all the internal interactions (QI and magnetic interaction) are aligned along the crystal axis. Hence implying, the proposed internal magnetic interaction due to spin polarization, if exists, is also aligned along the c-axis. In this work, the sample was placed in the 4-detector setup in the 0.5 T magnet pot with its c-axis lying in the detector plane, pointing at the start detector. In the R(t) spectra (Fig. 5.2 right) , an extremely damped frequency with a very small fraction is seen. This corresponds to the applied magnetic field and the earlier assumption of all internal interactions aligned along the c-axis still holds.

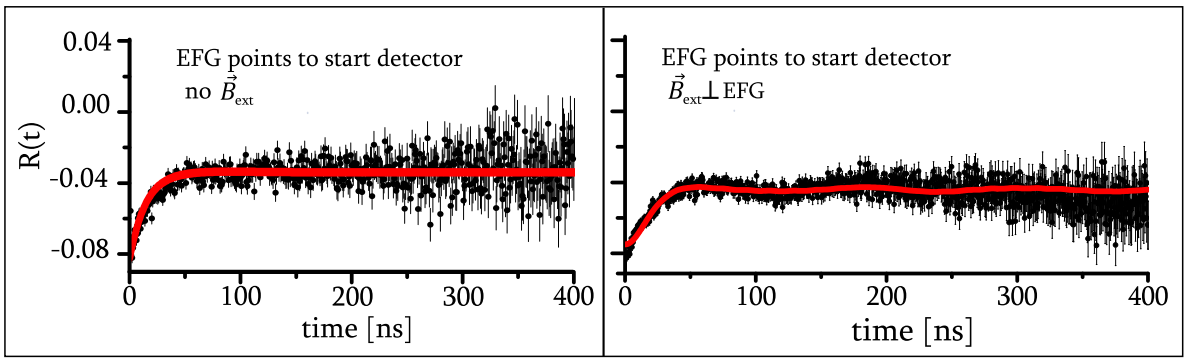

Figure 5.2: Left- past measurement with the c-axis pointing at the start detector (from PhD work of [Lor02]). Right- Same measurement but in the presence of an external magnetic field of 0.5 T with the $\vec{B_{ext}}$ perpendicular to the EFG (current work)

c-axis 45° Detector and c-axis ⊥ Detector Plane

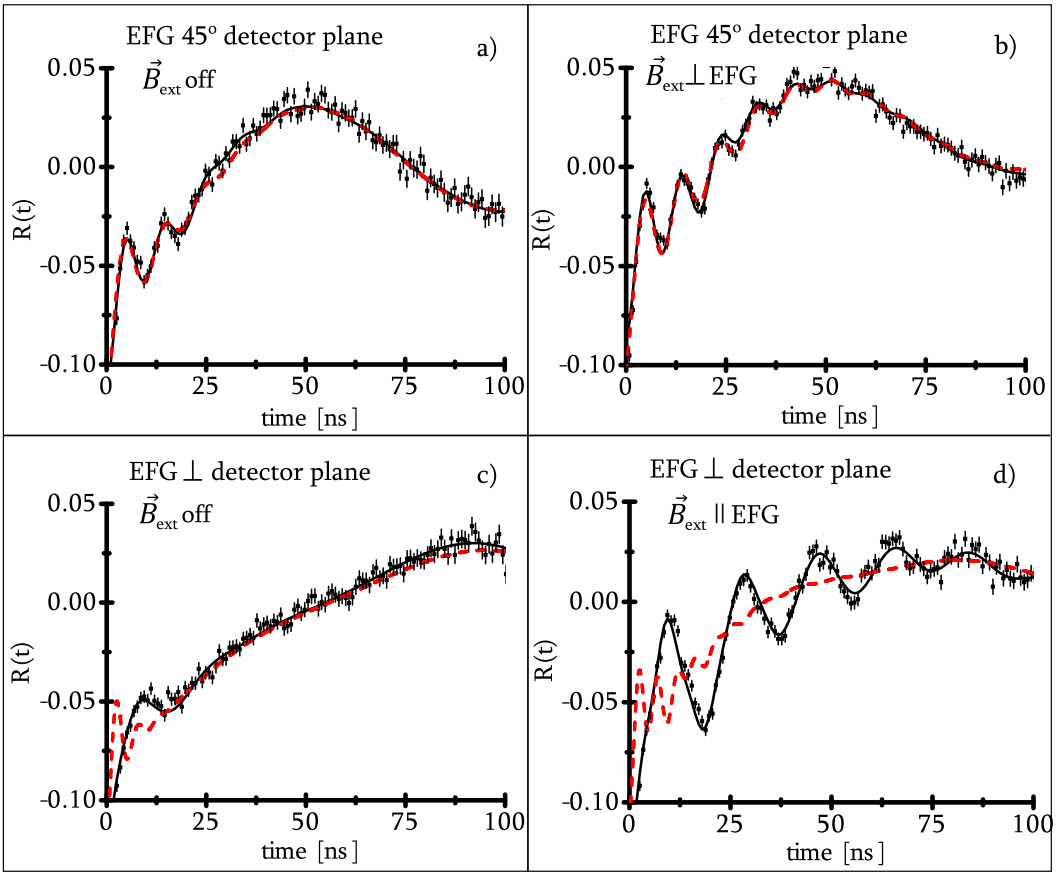

Figure 5.3: a) and c) are measurements without the external magnetic field and the b) and d) are measurements in the presence of the ≈0.5 T field. Measurements with c-axis 45° to the start detector are shown in the top row- a) and b) and with c-axis perpendicular to the detector plane are in the bottom row- c) and d). The solid black line are the fits based on suggested model (predominantly magnetic) and the dashed red (grey) line are fits assuming only a QI

Here a set of measurements were performed with the c-axis 45° degree to the start detector with and without $\vec{B}_{ext}$ in the magnet pot. This was followed by measurements with the c-axis oriented perpendicular to the detector plane. Here again, measurements were done with and without $\vec{B_{ext}}$. The recorded PAC spectra are shown in Fig. 5.3. The three expected frequencies are observed. In both the cases, f^{asym} is the smallest at $\sim 15\%$ followed by $f^{lat} \sim 35\%$ and f^{def} is maximum $\sim 50\%$. The latter two components are described as single crystalline fractions. In the 45° orientation measurement, the lattice frequency is smallest and is slightly damped while, the defect frequency is much faster and more damped. However, in the perpendicular measurement, the observed lattice frequency is clearly halved as before. The 45° measurement data was fitted according

to the suggested model and assuming only an EFG. As can be seen in Fig. 5.3, both the fits describe the data quite well. Following, the perpendicular measurements were fitted on the basis of the 45° measurement fit parameters. Here, the suggested model does not describe the data well but the EFG fit does. The fit parameters assuming a strong EFG are tabulated in Table. 5.1. The magnetic interaction data is tabulated in the Appendix....

	Orientation	ν_Q **(MHz)**	δ**(%)**	f_i**(%)**
Lattice	EFG **45°**, **0 T**	33.1(2)	5.1(3)	34.3(9)
	EFG **45°**, **0.5 T**	33.1(2)	5.5(3)	33.4(8)
	EFG ⊥, **0 T**	34.6(2)	3.1(3)	32.2(6)
	EFG ⊥, **0.5 T**	34.9(2)	1.4(3)	28.8(6)
defect	EFG **45°**, **0 T**	333(2)	18(1)	48(1)
	EFG **45°**, **0.5 T**	352(2)	10.6(5)	46.9(9)
	EFG ⊥, **0 T**	323(8)	47(2)	47.2(8)
	EFG ⊥, **0.5 T**	355(1)	6.4(2)	40.2(6)
Asymmetry	EFG **45°**, **0 T**	39.5(3)	18(2)	18(2)
	EFG **45°**, **0.5 T**	38.6(8)	19(2)	20(1)
	EFG ⊥, **0 T**	34.9(8)	22(1)	20.6(7)
	EFG ⊥, **0.5 T**	39.5(8)	27(2)	31.0(4)

Table 5.1: AlN fit parameters for 45° and ⊥ EFG orientations with and without $\vec{B}_{ext}$

5.1.2 Discussion- Orientation Measurement

For the case without $\vec{B}_{ext}$, on comparing the magnetic interaction and EFG fits of the strong interaction for the 45° geometry and the perpendicular geometry, it is clear the observed frequency in the case of 45° geometry is twice that in the case of perpendicular geometry. This is the case for a QI and the observed frequencies are ω_2 for 45° geometry and ω_1 for perpendicular geometry. The same trend is observed with $\vec{B}_{ext}$. This clearly establishes, the strong interaction is predominately due to a QI. Nevertheless, the presence of a weak magnetic interaction is still possible.

5.1.3 Discussion- Magnetic Effect

From the parameter Table 5.1 for strong QI, it is seen, 34.3(9)% - 28.9(6)% of the ^{111}In are at the defect free lattice environment and 48(1)% - 40.2(6)% at the V_N defect site. The assymetry fraction has $\eta = 0.51(7) - 0.62(1)$. The magnetic field of the 0.48(5) T magnet is found to be 0.47(1) T - 0.50(2) T from the fit parameters, well within the limits of experimental error. ν_Q^{lat} ranging from 34.6(1) MHz 34.8(2) MH, hardly showing any change under different magnetic conditions. While, ν_Q^{def} is observed to be 323(8) MHz and 333(2) MHz for the 45° and the perpendicular measurements respectively, it changes by almost 12% to 352(2) MHz and 355(1) MHz respectively. A strong dependence on the external magnetic field is clearly seen.

Again, for the lattice fraction, the change in δ^{lat} from 5.1(3)% to 5.5(4)% for 45° orientation and 3.1(3)% to 1.4(3)% for perpendicular orientation without and with $\vec{B}_{ext}$ respectively, is small. However, δ^{def} changes from 18(2)% to 10.6(5) % and from 47(2)% to 6.4(2)% under the same conditions as before. Here too, a dependence on an external magnetic field can be seen. Further, there seems to be a dependence of the influence on damping on the orientation of the EFG with respect to the applied field. This can be seen by comparing Fig. 5.3 a) with c) and Fig. 5.3 b) with d). When the EFG is oriented $\parallel$ to $\vec{B}_{ext}$, much less damping is observed as compared to the EFG$\perp$ $\vec{B}_{ext}$ orientation.

This trend of decrease in damping and increase in the QI frequency of the defect fraction is quite unexpected. It could be due to a weak internal magnetic interaction or a paramagnetic centre at the nitrogen site along the c-axis. A nearest neighbour V_N to the ^{111}In along the c-axis could be neutrally charged if it traps an electronic configuration (like an electron or polaron). This neutral charge state of the nitrogen vacancy donor is expected to be paramagnetic [EGH+06]. This could explain the spin alignment and hence, a more homogeneous probe lattice environment in the presence of an external magnetic field. Because the vacancy is associated to an electron configuration, the damping shows orientation dependence in the magnetic field.

5.2 GaN

5.2.1 Measurement

A GaN sample was measured 45° to the start detector with and without the 0.5 T magnetic field and ⊥ to the detector plane in the 2.1 T magnet pot. The observed R(t) spectra are shown in Fig. 5.4 and the fit parameters are tabulated in Table. 5.2. Here too, three frequencies are seen of which the f^{lat} and f^{def} are dominant. From the R(t) spectra, a strong influence of the magnetic field is observed on both the f^{lat} and f^{def}. In the 2.1 T magnetic field measurement, ω_L appears to be modulated by ω_Q.

5.2.2 Discussion

The spectra are fitted with two single crystalline fractions without η and one single crystalline fraction with a non zero η. Approximately, two thirds of the In atoms sit at the lattice site and one third at the defect site. The fitted magnetic field correspond to 0.51(1) T and 2.02(1) T for 0.48(5) T and 2.1 T magnets respectively, and are in good agreement with the theoretical values. The lattice fraction corresponds to a slow frequency $\nu_Q^{lat} = 5.61(7)$ MHz and the defect fraction to a slightly faster frequency $\nu_Q^{def} = 9.1(2)$ MHz. The QI strength at both these sites show little dependence on the applied field. The asymmetry fraction corresponds to a stronger QI and has $\eta = 0.1(6) - 0.65(5)$. Interestingly, like in the case of AlN, there is a dependence of damping on the magnetic field. The damping changes from 15(2)% to 10.9(9)% for 45° orientation and 28(2)% to 7.1(9)% for ⊥ orientation for f^{lat}. f^{def} sees a change from 34(4)% to 22(4)% for the 45° orientation and from 45(3)% to 5(5)% for the ⊥ orientation. Both show a significant dependence on the applied field. The change in δ^{lat} and ν_Q^{lat} is due to the combined interaction. Since ω_L and ω_Q are of the same order, a strong combined interaction affect is seen where the two frequencies superimpose each other. The same might be true for f^{def}, but since the ν_Q^{def} corresponds to ≈15 MHz, its dependence on $\vec{B}_{ext}$ could be due to a paramagnetic centre like in the case of AlN. In the 2.1 T measurement, since $\omega_L/\nu_Q \approx 5$ for f^{lat}, ω_L is observed in the R(t) modulated by ν_Q.

In these measurements, both f^{lat} and f^{def} are extremely damped resulting in large errors in the parameter values. Consequently, the unexpected variation in the parameter values

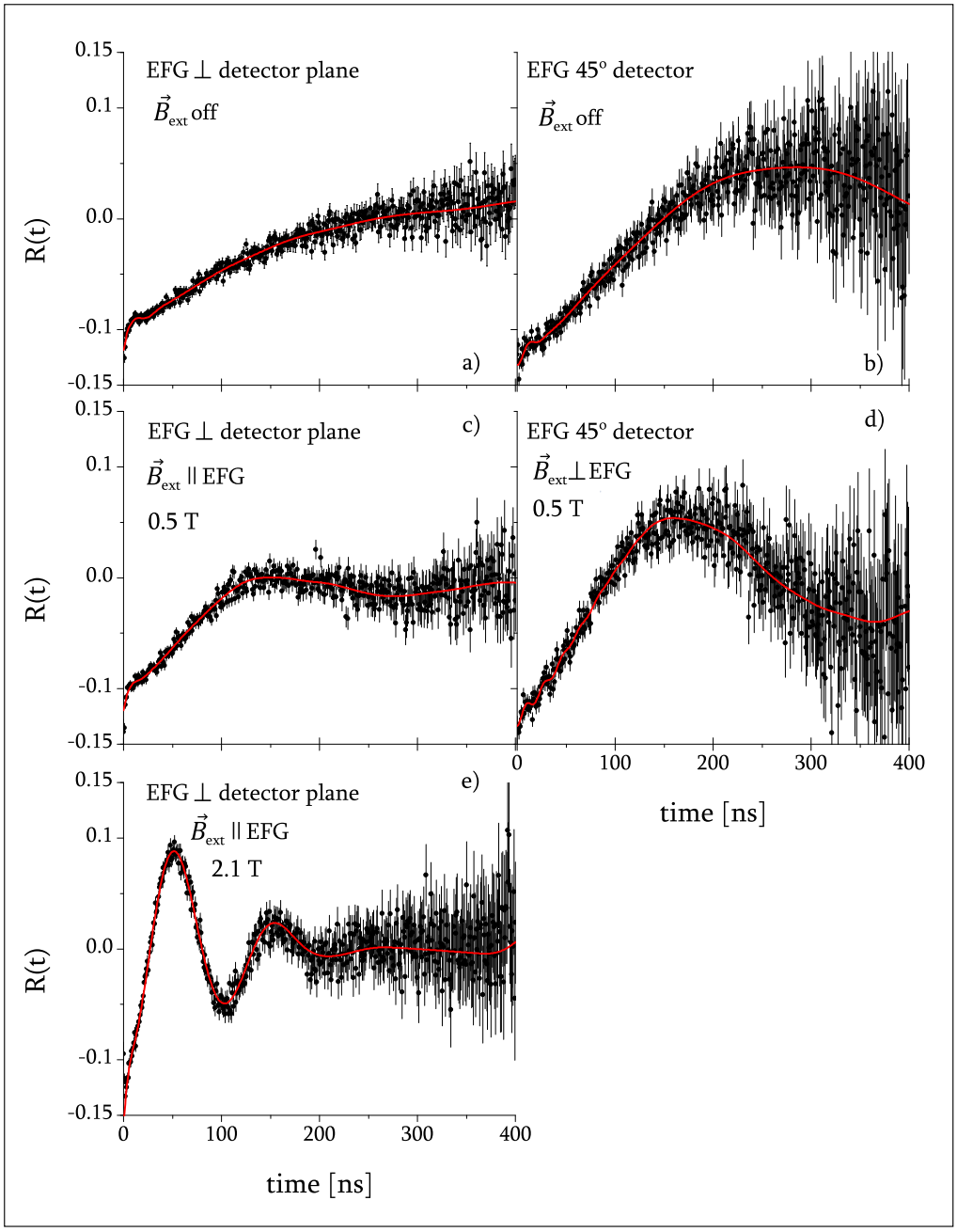

Figure 5.4: The first column contains measurements with the c-axis oriented perpendicular to the detector plane and the second column with c-axis 45° to the start detector. Measurements are performed in the absence of any external field, with 0.5 T and 2.1 T magnetic field

under different conditions could be due to these errors or could really exist. It is hard to say which is the case. But still, the possibility of magnetic affect should not be ignored.

	Orientation	ν_Q **(MHz)**	δ**(%)**	f_i**(%)**
Lattice	EFG **45°**, **0 T**	5.61(7)	15(2)	65(4)
	EFG **45°**, **0.5 T**	6.0(2)	10.9(9)	71(7)
	EFG ⊥, **0 T**	6.22(6)	28(2)	67(2)
	EFG ⊥, **0.5 T**	5.6(1)	7.1(9)	65(3)
	EFG ⊥, **2.1 T**	5.8(1)	7.1(9)	71(3)
defect	EFG **45°**, **0 T**	9.1(2)	34(4)	27(3)
	EFG **45°**, **0.5 T**	9.5(4)	22(4)	23(3)
	EFG ⊥, **0 T**	14.8(2)	45(3)	24.9(9)
	EFG ⊥, **0.5 T**	14.0(4)	29(4)	27(2)
	EFG ⊥, **2.1 T**	17.7(3)	5(2)	24(2)
Asymmetry	EFG **45°**, **0 T**	130(16)	26(6)	8(7)
	EFG **45°**, **0.5 T**	182(6)	4(3)	5.9(8)
	EFG ⊥, **0 T**	149(9)	19(6)	8.3(6)
	EFG ⊥, **0.5 T**	127(10)	14(7)	7.3(5)
	EFG ⊥, **2.1 T**	98(2)	11(6)	5.1(6)

Table 5.2: GaN fit parameters for 45° and ⊥ EFG orientations with and without $\vec{B}_{ext}$

Chapter 6

Summary

An attempt to understand the origin of the strong interaction observed in ^{111}In implanted AlN and GaN is made. The effect of an external magnetic field on the defect complex in these group III-nitrides is investigated. Measurements were done with ^{111}In implanted in AlN and GaN under different orientation conditions and under different external magnetic conditions. The measurement with the c-axis oriented to point at the start detector clearly shows the V_{zz} component of the crystal EFG is aligned along the c-axis. By comparing measurements of AlN oriented 45° to the start detector in detector plane and oriented $\perp$ to the detector plane, the nature of the strong interaction is determined to be dominantly electric. The model suggested in the past where the strong interaction is due to a defect complex between ^{111}In and a nearest neighbour V_N lying along the c-axis still stands. The proposed model with spin polarization calculations suggesting a strong magnetic field at the 111In/111Cd site will need to be revised.

In AlN, irrespective of the orientation, an effect of the external magnetic field on the lattice homogeneity is seen. This effect is restricted to the In-V_N defect complex lattice environment. It could be due to a probable paramagnetic nature of the nitrogen vacancy associated with an electric configuration (like a polaron). The influence of the magnetic field appears to have a preferential orientation since the homogeneity of the lattice seems to improve more when the samples EFG is aligned parallel to the external field as opposed to perpendicular. The magnetic effect is quite unexpected and very interesting as the magnetic field influences the In-V_N associated EFG.

The GaN measurements excellently demonstrate the combined interaction effect. With the 0.5 T measurement, due to similar field strengths, an equal contribution of the QI

and the magnetic interaction on the hyperfine splitting is seen. In the 2.1 T measurement, Zeeman Effect is dominant. A possibility of a similar magnetic effect as in the case of AlN exists, but it is hard to comment due to high damping.

Bibliography

[ABH+93] I. Alfter, E. Bodenstedt, B. Hamer, W. Knichel, R. Meler, R. Sajok, T. Schaefer, J. Schth, and R. Vianden. Core vibration of⁹⁹tc. *Zeitschrift fr Physik A Hadrons and Nuclei*, 347:1–14, 1993. 10.1007/BF01301270.

[AHP+80] A. R. Arends, C. Hohenemser, F. Pleiter, H. de Waard, L. Chow, and R. M. Suter. Data reduction methodology for perturbed angular correlation experiments. *Hyperfine Interactions*, 8:191–213, 1980. 10.1007/BF01026869.

[Bar92] N. P. Barrades. *NNFIT the PAC MANual*. Lissabon, 1992.

[Bez98] Eva Bezakova. *Implantation Damamge in Materials Studied by Hyperfine Interactions*. PhD thesis, Australian National University, 1998.

[BH80] J. P. Biersack and L. G. Haggmark. A monte carlo computer program for the transport of energetic ions in amorphous targerts. *Instruments and Methods*, 174:257–269, 1980.

[EGH+06] S. M. Evans, N. C. Giles, L. E. Halliburton, G. A. Slack, S. B. Schujman, and L. J. Schowalter. Electron paramagnetic resonance of a donar in aluminium nitride crystals. *Appl*, 88:062112, 2006.

[Ins] Ioffe Physico-Technical Institute. New semiconductor materials. characteristics and properties. Electronic archiv.

[KAN53] Ernst Heer Kurt Alder, H. Albers-Schoenberg and T. B. Novey. The measurement of nuclear moments of excited states by angular correlation method. i. *Helvetica Physica Acta*, 26:761–784, 1953.

[KAS63] Werner Schneider Kurt Alder, Eckart Matthias and Rolf M. Stefen. Influence of a combined magnetic dipole and electric quadrupole interaction on angular correlations. *Physical Review*, 129(3):1199, 1963.

[KLM+12] P. Kessler, K. Lorenz, S. M. C. Miranda, R. Simon, J. G. Correia, K. Johnston, R. Vianden, and ISOLDE Collaboration. Cd doping of aln via ion implantation studied with perturbed angular correlation. *physics ststus solidi (c)*, 9:1032–1035, 2012.

[Lor02] K. Lorenz. *Implantationsstudien an Gruppe-III-Nitriden*. PhD thesis, Rheinischen Friedrich -Wilhelms - Universität Bonn, 2002.

[LRV02] K. Lorenz, F. Ruske, and R. Vianden. Reversible changes in th elattice structure for in implanted gan. *Applied Physics Letters*, 80:4531–33, 2002.

[MÖ9] Krystyna Müller. Hyperfinewechselwirkungen von ^{100}pd in ru, ruo_2 and $ruga_3$. Master's thesis, Rheinischen Friedrich -Wilhelms - Universität Bonn, 2009.

[MSS62] Eckart Matthias, Werner Schneider, and Rolf M. Steffen. Nuclear level splitting caused by a combined electric quadrupole and magnetic dipole interaction. *Phys. Rev.*, 125:261–268, Jan 1962.

[NÓ7] Ronan Nédélec. *Seltene Erden in GaN und ZnO untursucht mit der PAC-Methode*. PhD thesis, Rheinischen Friedrich -Wilhelms - Universität Bonn, 2007.

[RR71] Pramila Raghavan and R. Raghavan. A new method for different perturbed angular correlation measurements. *Nuclear Instruments Methods*, 92:435, 1971. 10.1007/BF02354642.

[RR85] Pramila Raghavan and R. Raghavan. Hyperfine interaction studies with pulsed heavy-ion beams. *Hyperfine Interactions*, 26:855–888, 1985.

[Rus01] Florian Ruske. Indiumimplanation in galliumnitride untersucht mit der $\gamma-\gamma$-winkelkorrelationsmathode. Master's thesis, Rheinischen Friedrich -Wilhelms - Universität Bonn, 2001.

[Sie65] Kai Siegbahn. *Alpha-, Beta- and Gamma-Ray Spectroscopy*, volume 2. North-Holland Publishing Company, 1965.

[Sim11] R. Simon. Implantation studies on silicon doped group-iii nitride semiconductors. Master's thesis, Rheinischen Friedrich -Wilhelms - Universität Bonn, 2011.

[SNP+09] J. Schmitz, J Niederhausen, J. Penner, K. Lorenz, E. Alves, and R. Vianden. Stable in-defect complexes in gan and aln. *Physica B*, 404:4866–4869, 2009.

[SW96] G. Schatz and A. Weidinger. *Nuclear condensed matter physics: nuclear methods and applications*. John Wiley, 1996.

[Wu09] Junqiao Wu. When group-iii nitrides go infrared: New properties and perspectives. *Journal of Applied Physics*, 106:011101, 2009.

[ZJ11] Matthew Zacate and Herbert Jaeger. Perturbed angular correlation spectroscopy- a tool for the study of defects and diffusion at the atomic scale. *Defect and Diffusion Forum*, 311:3–38, 2011.